The study of eleven contact binaries with mass ratios less than 0.1

Xin-Yi Liu,[1] Kai Li,[1][⋆] Raul Michel,[2] Xiang Gao,[1] Xing Gao,[3] Fei Liu,[1] Shi-Peng Yin,[1] Xi Wang,[1] Guo-You Sun[4]

[1] *Shandong Key Laboratory of Optical Astronomy and Solar-Terrestrial Environment, School of Space Science and Physics, Institute of Space Sciences,*
Shandong University, Weihai, Shandong 264209, China
[2] *Observatorio Astronómico Nacional, Instituto de Astronomía, Universidad Nacional Autónoma de México, Apartado Postal 877, Ensenada, B.C. 22830, México*
[3] *Xinjiang Astronomical Observatory, 150 Science 1-Street, Urumqi 830011, China*
[4] *Wenzhou Astronomical Association, Beibaixiang Town, Yueqing, Zhejiang, 325603, China*

ABSTRACT

Multi-band photometric observations of eleven totally eclipsing contact binaries were carried out. Applying the Wilson-Devinney program, photometric solutions were obtained. There are two W-subtype systems, which are CRTS J133031.1+161202 and CRTS J154254.0+324652, and the rest systems are A-subtype systems. CRTS J154254.0+324652 has the highest fill-out factor with 94.3%, and the lowest object is CRTS J155009.2+493639 with only 18.9%. The mass ratios of the eleven systems are all less than 0.1, which means that they are extremely low mass ratio binary systems. We performed period variation investigation and found that the orbital periods of three systems decrease slowly, which may be caused by the angular momentum loss, and of six systems increase slowly, which indicates that the materials may transfer from the secondary component to the primary component. LAMOST low−resolution spectra of four objects were analyzed, and using the spectral subtraction technique, Hα emission line was detected, which means that the four objects exhibit chromospheric activity. In order to understand their evolutionary status, the mass-luminosity and mass-radius diagrams were plotted. The two diagrams indicate that the primary component is in the main sequence evolution stage, and the secondary component is above TAMS, indicating that they are over-luminous. To determine whether the eleven systems are in stable state, the ratio of spin angular momentum to orbital angular momentum (J_s/J_o) and the instability parameters were calculated, and we argued that CRTS J234634.7+222824 is on the verge of a merger.

Key words: binaries: close - binaries: eslipsing - stars: evolution – stars: individual

1 INTRODUCTION

In the field, open and globular clusters, contact binaries are usually observed (Rucinski 1994; Kaluzny 1990; Yan & Mateo 1994; Rubenstein & Bailyn 1996; Mazur et al. 1999). Rucinski (2002) estimated that there is one contact binary in every 500 main sequence stars. The large number of contact binaries provides abundant samples for studying the process of merging and the related physical mechanism, the phenomenon of materials transfer, and the presence of a third body (Eggleton & Kisseleva-Eggleton 2006). The two components are surrounded by the common envelope and hence have almost similar surface temperatures (Mochnacki 1981). There are two subtypes of contact binaries. The massive component of A-subtype binary is hotter, while the one of W-subtype binary is cooler (Binnendijk 1970). The common convection envelope (Lucy 1968) is located between the inner and outer critical equipotential surfaces, where the materials transfer occurs frequently. Short seperation of two components results in short periods and most systems are W UMa-type contact binaries with periods between 0.25 and 0.5 days (Sun et al. 2020). The most common explanation for the formation of W UMa-type contact binaries is that they are formed by the angular momentum loss (AML) of the initially detached systems through the magnetic wind (Maceroni & van't Veer 1996; McCarthy et al. 1996; Vilhu 1982; Qian 2003; Qian et al. 2017, 2018). The ultimate fate of the W UMa-type contact binaries may be to merge into a fast-rotating single object like FK Com-type star or blue straggler when the mass ratio is less than the instability mass ratio (q_{inst}) (Rasio 1995; Webbink 1976; Hut 1980; Eggleton & Kiseleva-Eggleton 2001). In open and globular clusters, a large number of W UMa-type contact binaries were discovered among blue stragglers, which confirmed this conjecture (Kaluzny & Shara 1988; Kaluzny 1990; Mateo et al. 1990; Yan & Mateo 1994).

Qian et al. (2005a) proposed that deep ($f > 50\%$), low mass ratio ($q < 0.25$) overcontact binaries may be the progenitors of blue straggler/ FK Com–type stars. If the the fill-out factor of overcontact binaries is quite high, exceeding 70% (Rasio & Shapiro 1995) or 86% (Li & Zhang 2006), dynamic instability will occur, and overcontact binaries will merge into a fast-rotating single star. The uncertainty of the value is due to the consideration of loss of angular momentum via gravitational wave radiation or magnetic stellar winds. So far, only one merged contact binary has been observed, that of V1309 Sco − Nova Sco 2008 (V1309 Sco) (Tylenda et al. 2011). Unfortunately, V1309 Sco was observed

---

⋆ E-mail: kaili@sdu.edu.cn

Table 1. The basic information of the eleven targets.

Target	Here after name	HJD$_0$	Period(days)	Vmax(mag)	Amplitude
CRTS J133031.1+161202	J133031	2459323.10154	0.3026661	13.17	0.27
CRTS J154254.0+324652	J154254	2459319.97154	0.3549879	14.90	0.25
CRTS J155009.2+493639	J155009	2459365.86122	0.4609100	13.61	0.20
CRTS J155106.5+303534	J155106	2459367.89252	0.3809891	14.88	0.22
CRTS J160755.2+332342	J160755	2459378.11819	0.3572878	15.13	0.26
CRTS J162327.1+031900	J162327	2459353.30508	0.4745615	13.74	0.22
CRTS J164000.2+491335	J164000	2459417.37225	0.3907817	13.47	0.25
CRTS J170307.9+020101	J170307	2459390.94490	0.2908836	13.29	0.21
CRTS J223837.9+321932	J223837	2459463.28323	0.4441697	13.82	0.23
CRTS J224827.6+341351	J224827	2459463.78173	0.3210262	14.87	0.21
CRTS J234634.7+222824	J234634	2459464.42501	0.2906934	13.82	0.23

after the merger event, so it is not possible to conduct targeted observations on it to study the properties and the merger mechanism of contact binaries. It is estimated that the Galactic rate of contact binaries mergers such as V1309 Sco is every 10 yr (Kochanek et al. 2014). Therefore, the identification of pre-merger candidates is of great significance for the monitoring of merger events of contact binaries.

Hut (1980) proposed that the instability (Darwin's instability) of contact binaries occurs when $J_o \leqslant 3J_s$, where J_o is the orbital angular momentum and J_s is the common spin angular momentum. Neglecting the spin angular momentum of the secondary, Rasio (1995) calculated that the q_{inst} (instability mass ratio) of the contact binary containing two unevolved main-sequence stars is 0.09. Considering the rotation of the secondary and using the dimensionless rotation radius of $k_1^2 = k_2^2 = 0.06$, Li & Zhang (2006) calculated the q_{inst} of the contact binary to be 0.071-0.078. Arbutina (2007) proposed a new criterion for calculating q_{inst}, that is, when $J_T = J_o + J_s$ reaches a critical value $dJ_T/dA = 0$, Darwin's instability will occur. Assuming $k_1^2 \neq k_2^2$ for the component's dimensionless gyration radii, Arbutina (2007) obtained the theoretical $q_{inst} = 0.094 - 0.109$ and when considering the effects of rotation, Arbutina (2009) obtained the theoretical $q_{inst} = 0.070 - 0.074$. Jiang et al. (2010) proposed that q_{inst} depends on the mass and structure of the primary, and it can be as low as 0.05. Many systems with extremely low mass ratios have been observed: M4 V53, $q \sim 0.078$ (Li et al. 2017); SX Crv, $q \sim 0.066$ (Rucinski et al. 2001), $q \sim 0.072$ (Zola et al. 2004); V857 Her, $q \sim 0.065$ (Qian et al. 2005b); V1187 Her, $q \sim 0.044$ (Caton et al. 2019); J082700, $q \sim 0.055$ and J132829, $q \sim 0.089$ (Li et al. 2021b). The discovery of these systems challenges the existing theories about the instability mass ratios of contact binaries. More observations and studies of contact binaries with mass ratios less than 0.1 are essential to refine the current theories.

Sun et al. (2020) performed a photometric analysis of 2335 late-type contact binaries extracted from the Catalina Sky Survey (CSS, Drake et al. 2014) and obtained their physical parameters, among which 112 contact binaries have mass ratios below 0.1. We selected some contact binaries with mass ratios lower than 0.1, performed photometric observations, and finally identified eleven totally eclipsing contact binaries with mass ratios less than 0.1. Table 1 listed the basic informations of the eleven contact binaries, including name, initial minimum moment, period, maximum magnitude of V-band, and amplitude. The V-band maximum magnitudes and amplitudes are from Drake et al. (2014). In this paper, we performed the photometric analysis of multiple-color light curves and investigations of orbital period changes of the eleven binary systems.

2 OBSERVATIONS

We conducted multi-band photometric observations on the eleven targets in six months (from April 2021 to September 2021), using 60cm Ningbo Bureau of Education and Xinjiang Observatory Telescope (NEXT), Weihai Observatory 1.0-m telescope of Shandong University (WHOT, Hu et al. (2014)), 85 cm telescope at the Xinglong Station of National Astronomical Observatories (NAOs85cm), the 84 cm telescope at the Observatorio Astronómico Nacional San Pedro Mártir (OAN-SPM). A back-illuminated FLI 230–42 CCD camera is used on NEXT. The CCD camera have 2048×2048 pixels, resulting in a field of view is $22' \times 22'$. A PIXIS 2048B CCD camera is equipped on WHOT. The scale of each pixel is approximately $0.35''$, which provides a field of view of about $12' \times 12'$. NAOs85cm uses an Andor DZ936 CCD camera. The scale of each pixel is approximately $0.94''$, which provides a field of view of about $32' \times 32'$. OAN-SPM equips an E2V back-illuminated CCD detector. The scale of each pixel is $0.26''$, which gives the field of view is $9' \times 9'$.

The observation time, observation band, exposure time and telescope used for each target are listed in Table 2. The observational error is about $10^{-3} - 10^{-2}$ mag. For data reduction, the data of WHOT, NAOs85cm and NEXT were processed by C-Munipack[1], and the OAN-SPM data were done with IRAF. The photometric images were performed bias, dark and flat corrections and processed with aperture photometry and differential photometry method. The differential magnitudes between the variable stars and the comparison stars and those between the comparison stars and the check stars were determined. The observation time and the differential magnitudes between the variable stars and the comparison stars are shown in Table A1. The selected comparison stars and check stars are also listed in Table 2.

---

[1] http://c-munipack.sourceforge.net/

Table 2. The observation details of the eleven contact binaries.

Target	Observaing Date	Exposure Time (s)	Comparsion Star	Check Star	Telescope
J133031	2021 Apr 18	V100 R45 I35	2MASS 13301646+1608087	2MASS 13300988+1606279	WHOT
J154254	2021 Apr 15	R40 I30	2MASS 15425099+3245591	2MASS 15430105+3251410	OAN-SPM
	2021 May 02	R80 I130	2MASS 15425099+3245591	2MASS 15430105+3251410	NAOs85cm
J155009	2021 May 31 June 03	B60 V25 R15 I15	2MASS 15503806+4937136	2MASS 15502157+4940514	OAN-SPM
	2021 June 28	B120 V60 R40 I35	2MASS 15503806+4937136	2MASS 15502157+4940514	WHOT
J155106	2021 June 02	R60 I50	2MASS 15505151+3036225	2MASS 15505887+3034427	OAN-SPM
	2021 July 10	R130 I120	2MASS 15505151+3036225	2MASS 15505887+3034427	WHOT
J160755	2021 July 01	R60 I50	2MASS 16080618+3322554	2MASS 16073601+3319151	OAN-SPM
	2021 July 12	R150 I130	2MASS 16080618+3322554	2MASS 16073601+3319151	WHOT
J162327	2021 May 09 18 22 23	g80 r70 i90	2MASS 16231038+0323098	2MASS 16234372+0319288	NEXT
	2021 June 15 17	g80 r70 i90	2MASS 16231038+0323098	2MASS 16234372+0319288	NEXT
J164000	2021 July 15 18 21 25	g65 r55 i75	2MASS 16400156+4916155	2MASS 16073601+3319151	NEXT
	2021 Aug 01 11	g65 r55 i75	2MASS 16400156+4916155	2MASS 16073601+3319151	NEXT
J170307	2021 June 24 25	V80 R40 I30	2MASS 17030255+0200346	2MASS 17031099+0200020	OAN-SPM
J223837	2021 Aug 11 18 25 Sep 05	g90 r75 i100	2MASS 22385725+3217007	2MASS 22384257+3215508	NEXT
J224827	2021 Sep 07 09	V80 R40 I40	2MASS 22484442+3416547	2MASS 22483392+3415584	OAN-SPM
J234634	2021 Sep 02 04 06	g80 r60	2MASS 23465840+2230443	2MASS 23463566+2222211	NEXT

Table 3. The information of spectra released by LAMOST and the equivalent width (EW) of Hα emission line.

Spectra	Date	T (K)	$\log g$	RV(km s^{-1})	[Fe/H]	SNR$_r$	EW(Å)
J133031	Apr.10 2013(1)	5946	4.050	34.52	-0.459	88	3.23(0.02)
	Apr.10 2013(2)	6004	4.127	20.20	-0.396	132	3.41(0.04)
	Feb.06 2016	5831	4.045	12.31	-0.417	92	3.80(0.13)
J154254	Mar.30 2019	5862	4.196	-35.05	-0.127	96	3.85(0.03)
J155009	Apr.24 2013	-	-	-	-	6	-
	Mar.25 2016	6907	3.948	-45.38	-0.099	14	-
J160755	Apr.22 2015	-	-	-	-	28	1.71(0.01)
J162327	Apr.24 2013	6942	4.205	-27.26	-0.442	37	3.72(0.11)
	Mar.25 2016	6899	4.248	-32.08	-0.402	71	5.71(0.13)

LAMOST (The Large Sky Area Multi-Object Fiber Spectroscopic Telescope, also known as the Goushoujing Telescope) is a special reflecting Schmidt telescope. Its field of view is 5° and it equipped 4000 fibers, which improve the rate of spectra acquisition (Cui et al. 2012; Zhao et al. 2012; Luo et al. 2015). The resolution is around 1800 for low resolution mode and the wavelength ranges from 3700 to 9000 Å(Du et al. 2016). We searched for objects in LAMOST Data Release 8 (DR8) for the low resolution mode using a matching radius of 2 arcsec and obtained the spectra of J133031, J154254, J155009, J160755, J162327. The information including the observational date, the effective temperature (T), surface gravity (log g), radial velocity (RV), metallicity abundance ([Fe/H]), signal noise ratio of r filter (SNR$_r$) of the five objects' spectra are shown in Table 3.

3 PHOTOMETRIC SOLUTIONS

In order to obtain the basic physical parameters of the eleven contact binaries, we used the 2013 version of the Wilson–Devinney (W-D) program (Wilson 1979, 1990; Wilson & Devinney 1971) to analyze their light curves. The effective surface temperature of the primary component is estimated by the colour indices and LAMOST data, considering the 3D extinction (Green et al. 2019). We calculated $g - r$, $B - V$, $J - K$ based on the magnitudes of B, V, g, r bands from AAVSO Photometric All Sky Survey (Henden et al. 2015) and J and K bands from 2MASS (Cutri et al. 2003). All the above mentioned temperatures and color indices are listed in Table 4. We took the average of all temperatures as the initial temperature of the primary component. Limb-darkening coefficients were obtained from the tables given by van Hamme (1993). When the system temperature is lower than 7200K, the gravity darkening and bolometric albedo coefficients were set to be $g_1 = g_2 = 0.32$, $A_1 = A_2 = 0.5$, otherwise, $g_1 = g_2 = 1$, $A_1 = A_2 = 1$ (von Zeipel 1924). For the eleven targets, the values of semi-major axis were set to be the values calculated by Equation (4) given in Li et al. (2022). J133031, J154254, J155009 and J162327 have non-solar chemical compositions and the values are found in LAMOST. For the four targets, the parameter of $[M/H]$ was set as the value determined by LAMOST in W-D program. In the process, the contact model (model 3) was adopted. The adjustable parameters are: the orbital inclination of the binary (i), the effective surface temperature of the secondary component (T_2), the dimensionless luminosity of each filter of the primary component (L_1), and the dimensionless surface potentials ($\Omega_1 = \Omega_2$).

In many cases, due to lack of radial velocity measurements, the q-search method was applied to determine the mass ratio. However, this may be inaccurate. But for the totally eclipsing contact binaries, the mass ratios are quite reliable. Pribulla et al. (2003) analysed the spectroscopic and photometric mass ratios of 80 contact binaries and found that they show some deviations in partially eclipsing binaries' data, and they are basically same in totally eclipsing binaries' data. Terrell & Wilson (2005) and Li et al. (2021a) proved this conclusion. Iterations were carried out using 0.1 step length between q=1 and q=5, 0.05 step length between q=0.2 and q=1, and 0.01 step length between q=0.01 and q=0.2, and during the process, the mass ratio was fixed. Then, we obtained a series of convergent solutions. The obtained convergent solutions of J154254 are only between q=0.07 and q=0.16. The sum square of residuals versus mass ratios are plotted and shown in Fig. 1. The mass ratio with the smallest residuals was selected as the initial mass ratio. Then we set mass ratio as an adjustable parameter. By running the W-D program, we got the photometric solutions. Due to the light curves of J133031, J154254, J155009, J170307, J224827, J234634 existing obvious O'Connell effect, we used the dark spot model to fit the distortion in the light curve. When using the dark spot model, the convergent solution is not unique. According to Eker (1999), the reasonable accuracy in spot parameters can be obtained when the photometric accuracy is 0.0001 mag or better. The photometric accuracy can't be so high, so the convergent solutions with dark spot we got are possible solutions. The convergent solutions determined by the above steps are preliminary solutions. Considering the spread of T_1 estimates leads to significant temperature and luminosity uncertainties, we used the following equations (Zwitter et al. 2003; Christopoulou & Papageorgiou 2013) to further determine the temperatures of two components,

$$T_1' = (((1 + k^2)T_1^4)/(1 + k^2(T_2/T_1)^4))^{0.25}$$
$$T_2' = T_1'(T_2/T_1)$$
(1)

where T_1 is the initial temperature of the primary component, T_2/T_1 and k are the temperature and the radius ratio, T_1' and T_2' are more accurate temperatures derived by Equation (1). We set more accurate temperatures derived by Equation (1) as initial values in W-D program, while the primary temperature was fixed and the secondary temperature was adjustable. By running the W-D program, convergent solutions were obtained after one iteration. Then, we set the values of semi-major axes obtained in Section 6 as initial values, and they were fixed in W-D program. By running the W-D program again, convergent solutions were obtained after one iteration. After obtaining convergent solutions, for eleven targets, the third light was set as an adjustable parameter, and running W-D program, only J223837 and J234634 obtained convergent solutions, while the other targets can't. The observed and theoretical light curves are shown in Fig. 2. The photometric solutions of the eleven targets are shown in Table 5. The relative errors of mass ratios we provided in Table 5 is about 0.1%, which is underestimated (Liu 2021; Terrell 2022). According to Liu (2021), if there is no third light, the relative errors of mass ratios of totally eclipsing contact binaries are about 1.0%, and when the third light exists, the relative errors will become larger, but less than 10.0%.

J133031, J154254, J155009, 155106, J164000 were observed by the Transiting Exoplanet Survey Satellite (TESS, Ricker et al. 2014). However, the datas of J154254 and 155106 are too poor, which may be caused by the target being too far from the center of the field of view, so we didn't use the data of the two targets for analysis. For J133031, J155009 and J164000, we set the obtained photometric solutions using our observations as initial parameters and ran the W-D program to get the photometric solutions and theoretical light curves of the TESS observation data. According to the 30 minutes observation cadence of TESS data, phase smearing effect was taken into account. After obtaining convergent solutions, the third light was set as an adjustable parameter, and running W-D program, J133031, J155009 and J164000 all obtained convergent solutions. However, the three targets of our data can't get convergent solutions when the third light parameter was adjustable in W-D program. This is because the scale of our data is very small and the scale of TESS data is 21 arcsec, when observing targets, the nearby companion stars will be included. Therefore, we searched J133031, J155009 and J164000 in Gaia DR3 (Gaia Collaboration et al. 2016, 2022; Babusiaux et al. 2022) using matching radius of 10 arcsec and 42 arcsec. When using a matching radius of 10 arcsec, no companion objects have been found, so it is correct that the three targets of our data can't get convergent solutions when the third light parameter was adjustable in W-D program. When using a matching radius of 42 arcsec, we found that J133031 exists three companion objects, J155009 exists one companion object and J164000 exists two companion objects. According to the magnitude given by Gaia DR3, we calculated flux ratios of third light flux to total flux using the following equation.

$$m_2 - m_1 = -2.5lg(E_2/E_1)$$
(2)

The observed and theoretical light curves are shown in Fig. 3. The photometric solutions of TESS data and flux ratios calculated by Equation (2) are shown in Table 6. It is found that flux ratios obtained from the light curve analysis using W-D program are close to the ratios calculated by Equation (2). It should be noted that we use solutions obtained from our data as final solutions for the discussion in Section 6.

4 ORBITAL PERIOD INVESTIGATIONS

The study of orbital period variation is of great significance for discussing the dynamic interaction of the binary systems, the existence of a third body and the materials transfer between the two components of binary systems (Zhou et al. 2016; Er-gang et al. 2019; Li et al. 2018; Liao et al. 2019; Pi et al. 2019). Therefore, the research of the orbital period variation has always been an important part of the binary systems. We collected minimum moments of the eleven targets as many as possible from our observation data and sky survey data bases including the All-Sky Automated Survey for SuperNovae (ASAS-SN, Shappee et al. 2014; Kochanek et al. 2017), the Zwicky Transient Facility (ZTF) survey (Bellm et al. 2018; Masci et al. 2018), Wide Angle Search for Planets (WASP, Butters et al. 2010), CSS and TESS. Data from ASAS-SN, ZTF and CSS is discrete and the observation cadence of TESS is 30 minutes, hence their minimum moments can't be obtained directly. In

Table 4. The effective surface temperature of the eleven targets' primary components.

Target	$(g-r)_0$	$(B-V)_0$	$(J-K)_0$	T_{g-r}(K)	T_{B-V}(K)	T_{J-K}(K)	T_{LAMOST}(K)	T_{eff}(K)
J133031	0.40	0.58	0.41	5990	5990	5550	5831/5946/6004	5880
J154254	0.40	0.61	0.35	5990	5930	5860	5862	5910
J155009	0.27	0.48	0.24	6550	6350	6550	6907	6580
J155106	0.09	0.22	0.27	7220	7760	6350	-	7110
J160755	0.07	0.24	0.02	7400	7590	8800	-	7930
J162327	0.15	0.14	0.18	7020	6640	6810	6942/6899	6860
J164000	0.15	0.35	0.13	7020	6820	7400	-	7080
J170307	0.58	0.72	0.48	5480	5480	5270	-	5410
J223837	0.15	0.32	0.22	7020	7020	6670	-	6900
J224827	0.29	0.56	0.38	6350	6050	5660	-	6020
J234634	0.43	0.59	0.38	5930	5930	5680	-	5840

Table 5. Photometric Solutions

Target	J133031	J154254	J155009	J155106	J160755	J162327	J164000	J170307	J223837	J224827	J234634
T_1'(K)	5860	5885	6619	7147	7987	6914	7137	5433	6919	6077	5851
T_2'(K)	6019(12)	6067(16)	6199(16)	6819(21)	7476(62)	6380(18)	6574(18)	5237(15)	6756(25)	5541(27)	5746(13)
i	88.3(2)	84.4(3)	85.7(2)	74.8(5)	74.9(6)	82.5(4)	83.5(2)	75.7(4)	74.0(3)	83.2(6)	74.6(3)
$q(M_2/M_1)$	0.0980(4)	0.0867(2)	0.0815(7)	0.0885(15)	0.0991(23)	0.0968(8)	0.0951(7)	0.0930(12)	0.0933(11)	0.0791(4)	0.0855(6)
Ω	1.917(2)	1.863(1)	1.890(4)	1.883(7)	1.933(8)	1.932(4)	1.926(4)	1.895(5)	1.911(5)	1.845(1)	1.893(3)
$(L_1/L_t)_B$	—	—	0.930(1)	—	—	—	—	—	—	—	—
$(L_1/L_t)_V$	0.867(1)	—	0.924(1)	—	—	—	—	0.901(1)	—	0.928(1)	—
$(L_1/L_t)_R$	0.869(1)	0.871(1)	0.921(1)	0.902(1)	0.903(1)	—	—	0.898(1)	—	0.923(1)	—
$(L_1/L_t)_I$	0.871(1)	0.873(1)	0.918(1)	0.899(1)	0.899(1)	—	—	0.896(1)	—	0.919(1)	—
$(L_1/L_t)_g$	—	—	—	—	—	0.920(1)	0.922(1)	—	0.820(1)	—	0.896(1)
$(L_1/L_t)_r$	—	—	—	—	—	0.913(1)	0.914(1)	—	0.852(1)	—	0.895(1)
$(L_1/L_t)_i$	—	—	—	—	—	0.909(1)	0.910(1)	—	0.863(1)	—	—
$(L_3/L_t)_g$	—	—	—	—	—	—	—	—	0.086(15)	—	0.009(11)
$(L_3/L_t)_r$	—	—	—	—	—	—	—	—	0.048(16)	—	0.008(10)
$(L_3/L_t)_i$	—	—	—	—	—	—	—	—	0.034(17)	—	—
r_1	0.599(1)	0.618(1)	0.603(1)	0.608(3)	0.592(2)	0.592(1)	0.593(1)	0.606(2)	0.599(2)	0.623(1)	0.604(1)
r_2	0.225(4)	0.239(6)	0.199(8)	0.226(23)	0.220(20)	0.213(7)	0.212(7)	0.229(17)	0.218(11)	0.229(8)	0.209(7)
f	0.560(27)	0.943(12)	0.189(71)	0.693(124)	0.361(36)	0.274(64)	0.287(60)	0.698(86)	0.449(78)	0.916(22)	0.373(56)
$Spot$	star1	star1	star1	—	—	—	—	star1	—	star1	star1
$\theta(deg)$	29.14(76)	104.90(154)	165.08(48)	—	—	—	—	133.99(83)	—	113.34(181)	120.08(39)
$\lambda(deg)$	295.66(190)	251.78(111)	0.35(219)	—	—	—	—	48.30(194)	—	24.24(263)	81.30(81)
$r_s(deg)$	17.22(25)	14.87(17)	31.21(29)	—	—	—	—	16.69(30)	—	19.86(42)	19.86(13)
T_f	0.81(1)	0.81(1)	0.85(1)	—	—	—	—	0.71(2)	—	0.93(1)	0.83(1)

order to derive as many minimum moments as possible, we used the method proposed by Li et al. (2020) to obtain the minimum moments. All minimum moments, errors and their sources are listed in Table 7.

We calculated the values of O–C employing the following equation,

$$BJD = BJD_0 + P \times E \qquad (3)$$

where BJD is the minimum moment, BJD_0 is the initial minimum moment, P is period, and E is cycle number. All initial minimum moments and periods are listed in Table 1. All initial minimum moments listed in Table 1 are HJD, and we transformed them from HJD to BJD on the website[2]. The general trends of O-C curves are obtained and shown in Fig. 4. According to the least squares method, we made linear fitting and quadratic fitting to the O-C curves. In order to determine which fitting is better, we calculated AIC and BIC values based on the two fittings. The criteria are defined as follows,

$$AIC = nlog(RSS/n) + 2k$$

$$BIC = nlog(RSS/n) + klogn \qquad (4)$$

where n is the number of data points and k is the number of parameters estimated by the model. The smaller of the AIC and BIC values,

---

[2] http://astroutils.astronomy.ohio-state.edu/time/hjd2bjd.html
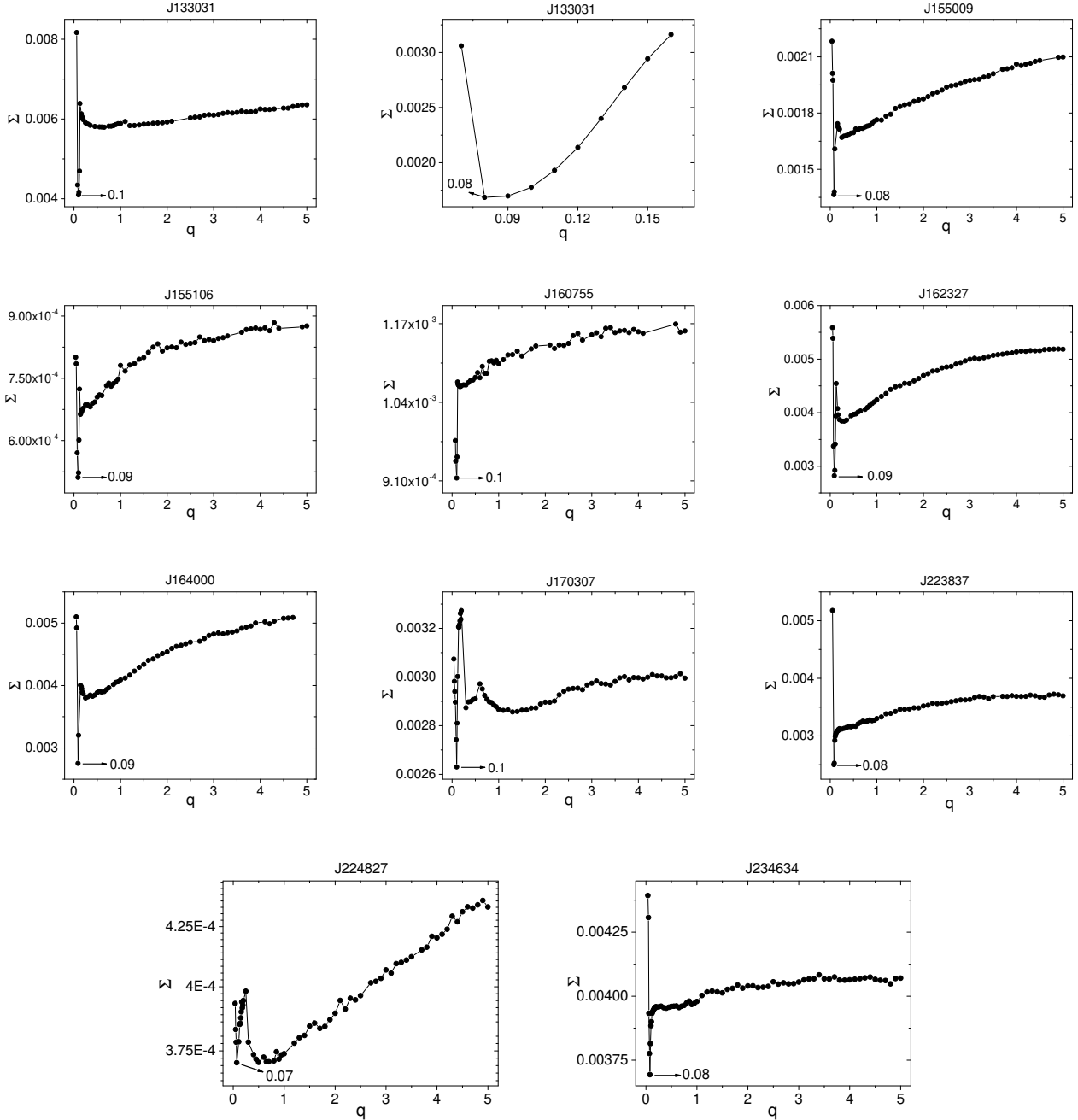
Figure 1. This figure displays the sum square of residuals Σ versus mass ratio q.

the better of the fitting result. The corrected values of initial minimum moments and period are shown in Table 8. We found that the general trend of the O-C curves of J133031, J160755 and J162327 is straight line, of J155109, J170307, J223837, J224827 and J234634 is an upward parabola, which means that the period is slowly increasing, and of J154254, J155106 and J164000 is a downward parabola, which means that the period is slowly decreasing.

5 SPECTRA ANALYSIS

Most W UMa-type eclipsing binaries may be chromospherically active binaries, because the spectral types of the two components are later than F (Eker et al. 2008). An important indicator of chromospheric activity is the presence of Hα (6563Å) emission line (Hall 2008). Hα emission line can be applied as the optical and near-infrared diagnostics of stellar chromospheric activity in late type rotating stars (Wilson

Table 6. Photometric solutions of TESS datas

Target	J133031-1	J133031-2	J155009	J164000
$T_1(K)$	5860	5860	6619	7137
$T_2(K)$	6256(9)	6018(11)	6079(7)	6495(8)
i	87.9(3)	79.4(4)	86.2(1)	87.9(1)
$q\,(M_2/M_1)$	0.1082(8)	0.0910(2)	0.0824(4)	0.0995(2)
Ω	1.946(4)	1.872(1)	1.884(2)	1.938(1)
(L_1/L_t)	0.831(1)	0.868(2)	0.885(1)	0.895(1)
(L_3/L_t)	0.015(13)	—	0.035(5)	0.015(5)
$(L_3/L_t)_{Gaia}$	0.046	—	0.014	0.007
r_1	0.591(1)	0.616(1)	0.606(1)	0.590(1)
r_2	0.232(8)	0.250(11)	0.205(4)	0.215(2)
f	0.540(52)	0.985(11)	0.350(29)	0.287(21)
$Spot$	star1	star1	—	—
$\theta(deg)$	115.93(104)	152.77(51)	—	—
$\lambda(deg)$	89.76(109)	27.89(176)	—	—
$r_s\,(deg)$	15.97(14)	25.85(31)	—	—
T_f	0.84(1)	0.81(1)	—	—

Table 7. The minimum moments of eleven contact binaries.

Target	BJD	Error	Min	Epoch	O-C	Residuals	Ref
J133031	2456856.98783	0.00061	p	-8148	0.00884	-0.00152	(1)
	2456856.83570	0.00073	s	-8148.5	0.00804	-0.00232	(1)
	2458269.83219	0.00061	p	-3480	0.00784	0.00419	(2)
	2458269.98242	0.00041	s	-3479.5	0.00674	0.00309	(2)
	2458561.90067	0.00076	p	-2515	0.00354	0.00127	(2)
	2458562.05258	0.00122	s	-2514.5	0.00411	0.00185	(2)
	2458962.93344	0.00118	p	-1190	0.00372	0.00336	(2)
	2458963.07890	0.00113	s	-1189.5	-0.00215	-0.00251	(2)
	2459269.07260	0.00101	s	-178.5	-0.00387	-0.00278	(2)
	2459269.22821	0.00083	p	-178	0.00040	0.00150	(2)
	2458283.75483	0.00061	p	-3434	0.00784	0.00426	(2)
	2458283.90540	0.00033	s	-3433.5	0.00708	0.00350	(2)
	2458573.85709	0.00057	s	-2475.5	0.00465	0.00244	(2)
	2458574.00739	0.00072	p	-2475	0.00361	0.00141	(2)
	2458899.07456	0.00080	p	-1401	0.00740	0.00673	(2)
	2458899.21834	0.00116	s	-1400.5	-0.00016	-0.00082	(2)
	2459291.92714	0.00064	p	-103	-0.00062	0.00058	(2)
	2459292.07438	0.00073	s	-102.5	-0.00472	-0.00351	(2)
	2458547.97803	0.00096	p	-2561	0.00354	0.00121	(2)
	2453827.89995	0.00209	p	-18156	0.00329	-0.02146	(3)
	2453828.06695	0.00213	s	-18155.5	0.01896	-0.00579	(3)
	2454949.93652	0.00394	p	-14449	0.05662	0.03720	(3)
	2454950.09233	0.00270	s	-14448.5	0.06110	0.04168	(3)
	2456062.90590	0.00217	s	-10771.5	-0.02857	-0.04271	(3)
	2456063.04713	0.00324	p	-10771	-0.03868	-0.05281	(3)
	2459323.10237	0.00075	p	0	0.00000	0.00135	(4)
	2459323.25146	0.00037	s	0.5	-0.00224	-0.00089	(4)
	2458932.51436	0.00021	s	-1290.5	0.00259	0.00213	(5)
	2458932.66292	0.00023	p	-1290	-0.00018	-0.00064	(5)
	2458938.56630	0.00021	s	-1270.5	0.00121	0.00078	(5)
	2458938.71520	0.00013	p	-1270	-0.00123	-0.00165	(5)
	2458948.25108	0.00025	s	-1238.5	0.00067	0.00029	(5)
	2458948.40102	0.00018	p	-1238	-0.00072	-0.00110	(5)
	2458952.63938	0.00012	p	-1224	0.00031	-0.00004	(5)
	2458952.79101	0.00020	s	-1223.5	0.00061	0.00025	(5)

(1)ASAS-SN; (2)ZTF; (3)CSS; (4)WHOT; (5)TESS; (6)WASP (7) OAN-SPM (8)NAOs85cm (9)NEXT

This table is available in its entirety in machine-readable form in the online version of this article.
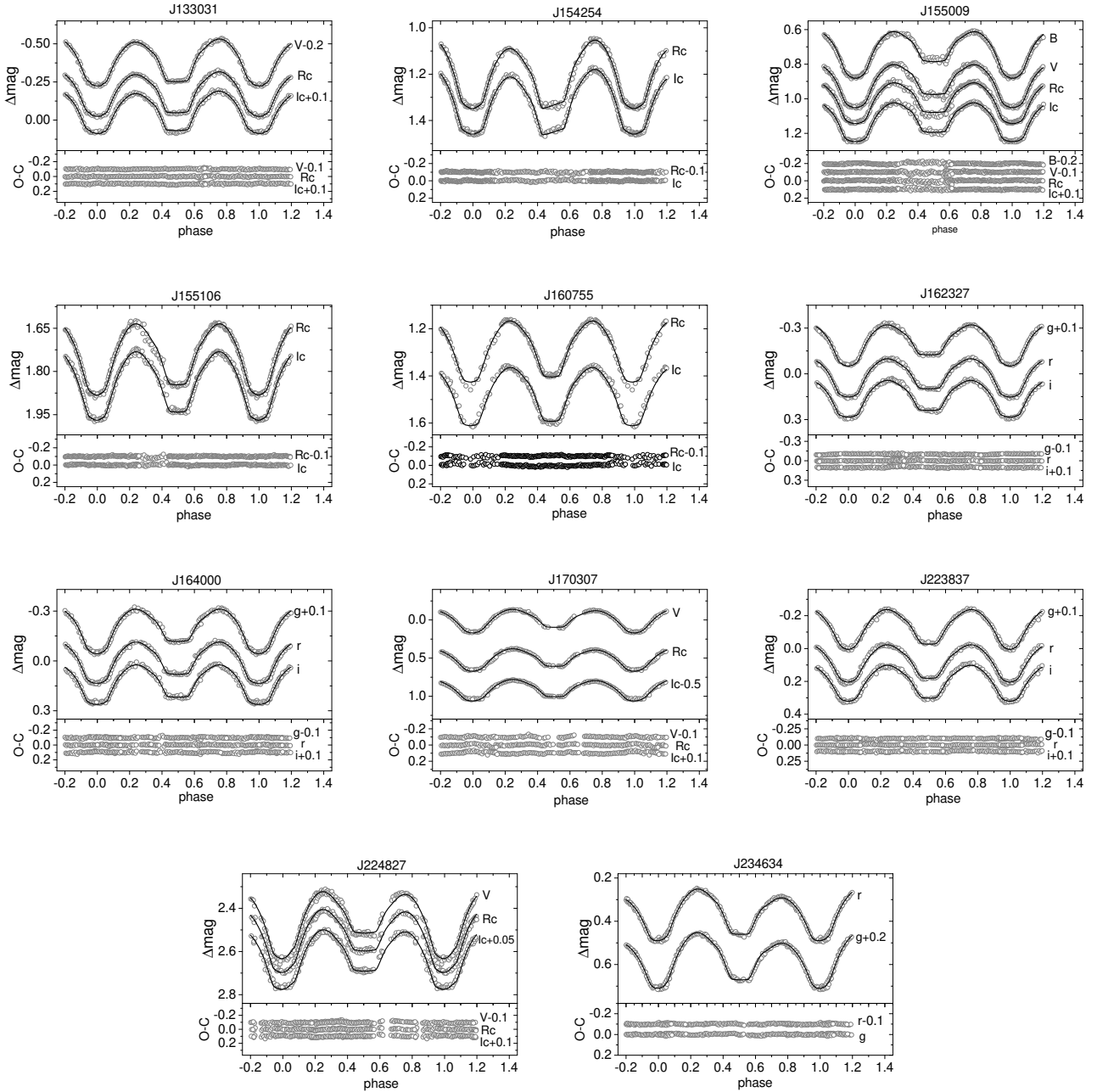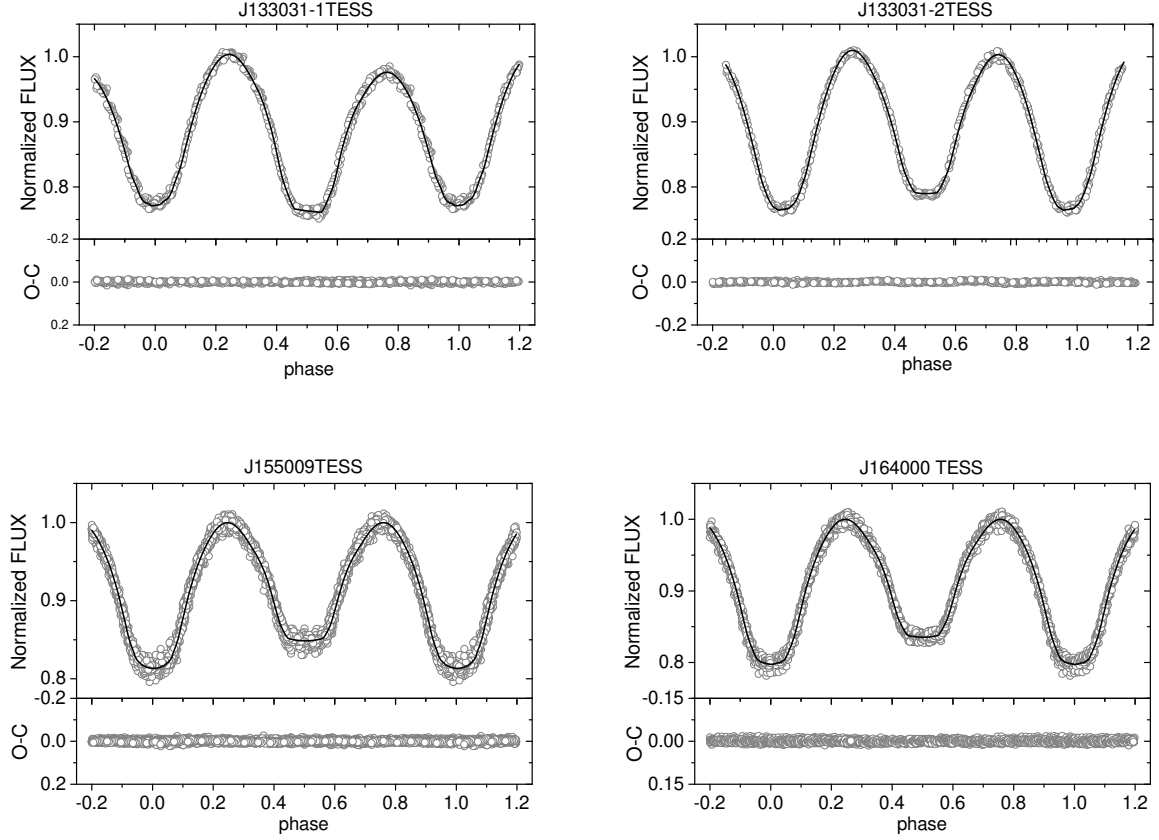
Figure 2. This figure displays observed (symbols) and theoretical (solid lines) light curves.

1978; Barden 1984; Montes et al. 1995). In order to determine whether J133031, J154254, J155009, J160755, J162327 exist chromospherical activity, we analyzed their spectra. Due to the low SNR of J155009' spectra (shown in Table 3), we didn't use them for the following analysis.

We performed flux normalization and decosmic ray processing on the spectra. In order to analyze Hα emission line, the spectra subtraction technique performed by Barden (1985) was adopted. The template spectra was generated using the iSpec [3] software package according to temperatures and log g (shown in Table 3). According to the redshift of the object spectra, we shifted the template spectra to keep the corresponding spectral line wavelengths are consistent. The subtracted spectra were obtained by subtracting the inactive synthesized spectra from the object spectra. The object, synthesized and subtracted spectra are shown in Fig. 5. We identified the Hα emission line from the subtracted spectra of Fig. 5. The equivalent width (EW) of the Hα emission line was obtained using the splot command in the iraf package and shown in Table 3. The existence of Hα emission line indicates that J133031, J154254, J160755, J162327 exist chromospheric activity.

---

[3] https://iscottmark.gitee.io/iSpec/

Figure 3. This figure displays observed (symbols) and theoretical (solid lines) light curves of TESS observation data.

Table 8. The corrected values based on O-C analysis.

Target	Lin fit*		Qua fit*		ΔT_0	ΔP	dP/dt	dM_1/dt	τ	τ_{th}
	AIC	BIC	AIC	BIC	$(\times 10^{-4} days)$	$(days)$	$(d\,yr^{-1})$	$(M_\odot yr^{-1})$	yr	yr
J133031	-122.7	-123.6	-119.9	-121.3	-14.20(6.50)	$-1.45(0.33) \times 10^{-6}$	-	-	-	-
J154254	-122.4	-123.4	-125.2	-126.6	-21.30(16.40)	$-4.10(0.53) \times 10^{-10}$	$-1.11(0.17) \times 10^{-2}$	-1.31×10^{-3}	1.01×10^3	1.16×10^7
J155009	-102.0	-103.3	-114.8	-116.8	2.22(8.41)	$3.93(0.91) \times 10^{-10}$	$9.28(1.36) \times 10^{-3}$	9.52×10^{-4}	-	-
J155106	-124.9	-126.0	-142.3	-144.0	14.00(6.48)	$-2.67(0.24) \times 10^{-10}$	$-7.56(0.66) \times 10^{-3}$	-8.88×10^{-4}	1.56×10^3	1.02×10^7
J160755	-79.2	-80.8	-78.0	-80.4	40.70(7.15)	$-3.32(0.91) \times 10^{-7}$	-	-	-	-
J162327	-82.8	-84.7	-81.3	-83.7	-6.42(6.81)	$7.87(1.37) \times 10^{-7}$	-	-	-	-
J164000	-410.3	-410.5	-426.2	-426.4	0.33(3.65)	$-1.71(0.18) \times 10^{-10}$	$-6.51(4.74) \times 10^{-4}$	-8.09×10^{-5}	1.71×10^4	1.00×10^7
J170307	-90.8	-92.2	-102.3	-104.4	7.11(5.82)	$1.01(0.12) \times 10^{-10}$	$1.11(0.57) \times 10^{-3}$	1.58×10^{-4}	-	-
J223837	-105.9	-107.2	-110.6	-112.2	-0.04(8.73)	$3.21(0.41) \times 10^{-10}$	$8.83(0.77) \times 10^{-3}$	9.40×10^{-4}	-	-
J224827	-105.5	-106.8	-105.7	-107.7	8.67(10.00)	$3.39(2.42) \times 10^{-11}$	$1.61(0.99) \times 10^{-3}$	1.78×10^{-4}	-	-
J234634	-124.3	-125.4	-129.1	-130.8	-3.06(8.53)	$8.72(1.53) \times 10^{-11}$	$3.50(0.77) \times 10^{-3}$	3.91×10^{-4}	-	-

*Lin fit: linear fitting; *Qua fit: quadratic fitting.

6 DISCUSSTIONS AND CONCLUSIONS

Muti-band photometry and spectra analysis were carried out to get the eleven contact binaries' physical and absolute parameters. Applying the W-D program, the photometric solutions were obtained. Due to the obvious O'Connell effect existing in the light curves of J133031, J154254, J155009, J170307, J224827 and J234634, we used the dark spot model to fit the distortion in the light curves. The mass ratios of the eleven contact binaries are all less than 0.1 and reliable because these systems are totally eclipsing binary systems (Pribulla et al. 2003; Terrell & Wilson 2005; Li et al. 2021a). There are two W-subtype binary systems, they are J133031 and J154254, while the rest binary systems are A-subtype binary systems. Among the eleven systems, J164000 has the largest temperature difference between the two components, which is
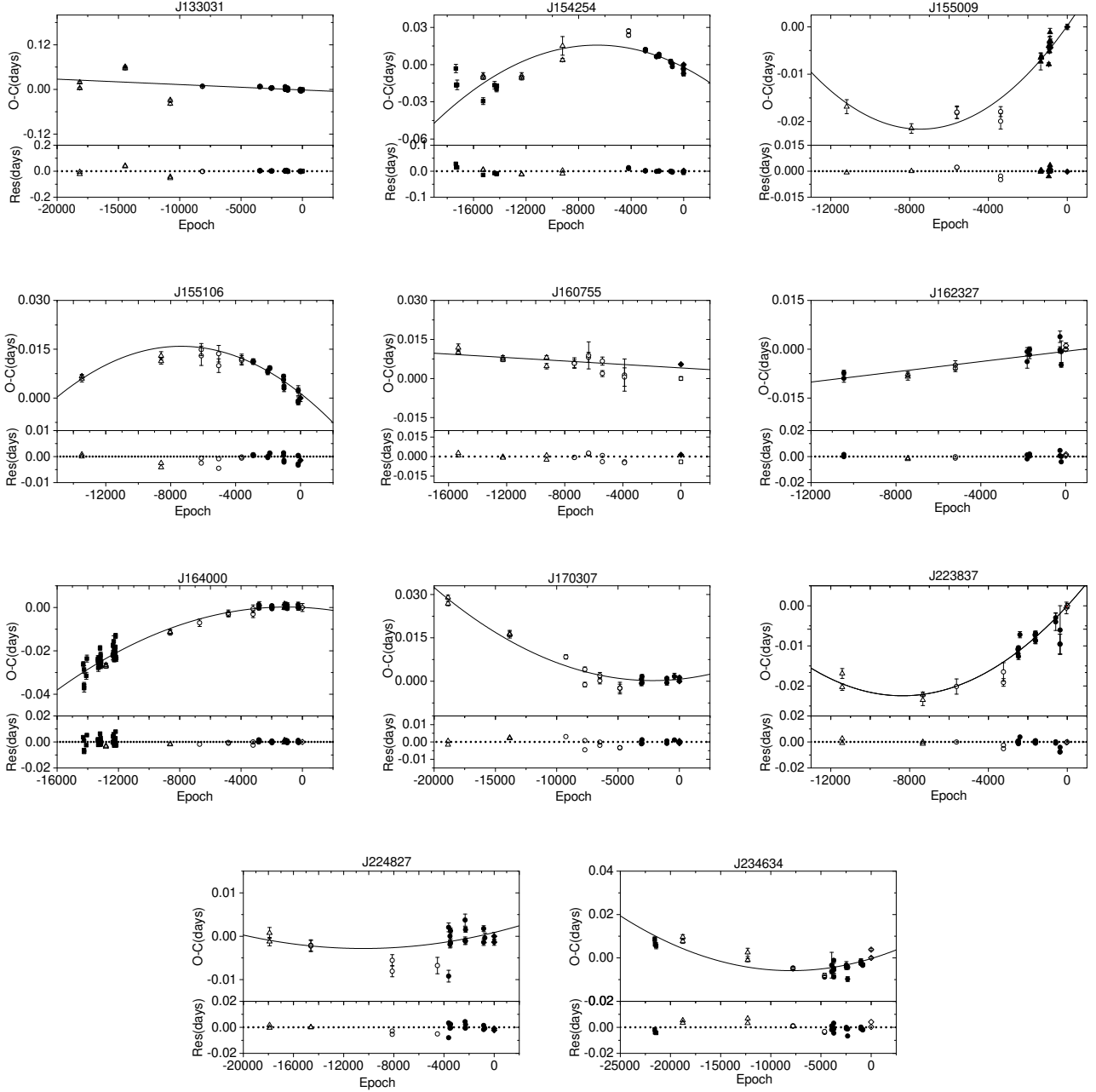
Figure 4. This figure depicts the O−C values. The residuals are shown at the bottom of the figure. ZTF •; ASAS-SN ◦; TESS ▲; CSS △; WASP ■; WHOT □; OAN-SPM ◆; NEXT ◇; NAOs85cm ★

563K. Christopoulou et al. (2022) proposed a conclusion that contact binaries with low-mass ratios can present deep or medium or shallow degree of contact. Qian et al. (2005a) defined that the contact binaries whose degree of contact exceeds 50% as deep contact binaries.We defined medium and shallow contact configuration as that the fill-out factors are between 25% and 50%, and less than 25%. According to the photometric solutions, we knew that the fill-out factors of eleven targets are between 18.9% and 94.3%, which showed that our contact binaries have shallow, medium and deep contact systems. Therefore, it proved the conclusion proposed by Christopoulou et al. (2022). Table 9 listed the physical parameters obtained by us and those determined by Sun et al. (2020). We compared these parameters and found that the mass ratios are similar, the fill-out degree and the inclination are quite different, and the errors of Sun et al. (2020) are generally large. Our photometric accuracy is better, the quality of sky survey data is relatively poor, and multi-band photometry are used by us. Therefore, to a certain extent, we believed that our results are more reliable.

According to the three-dimensional correlations provided by (Gazeas 2009), the absolute parameters of the two components of the eleven
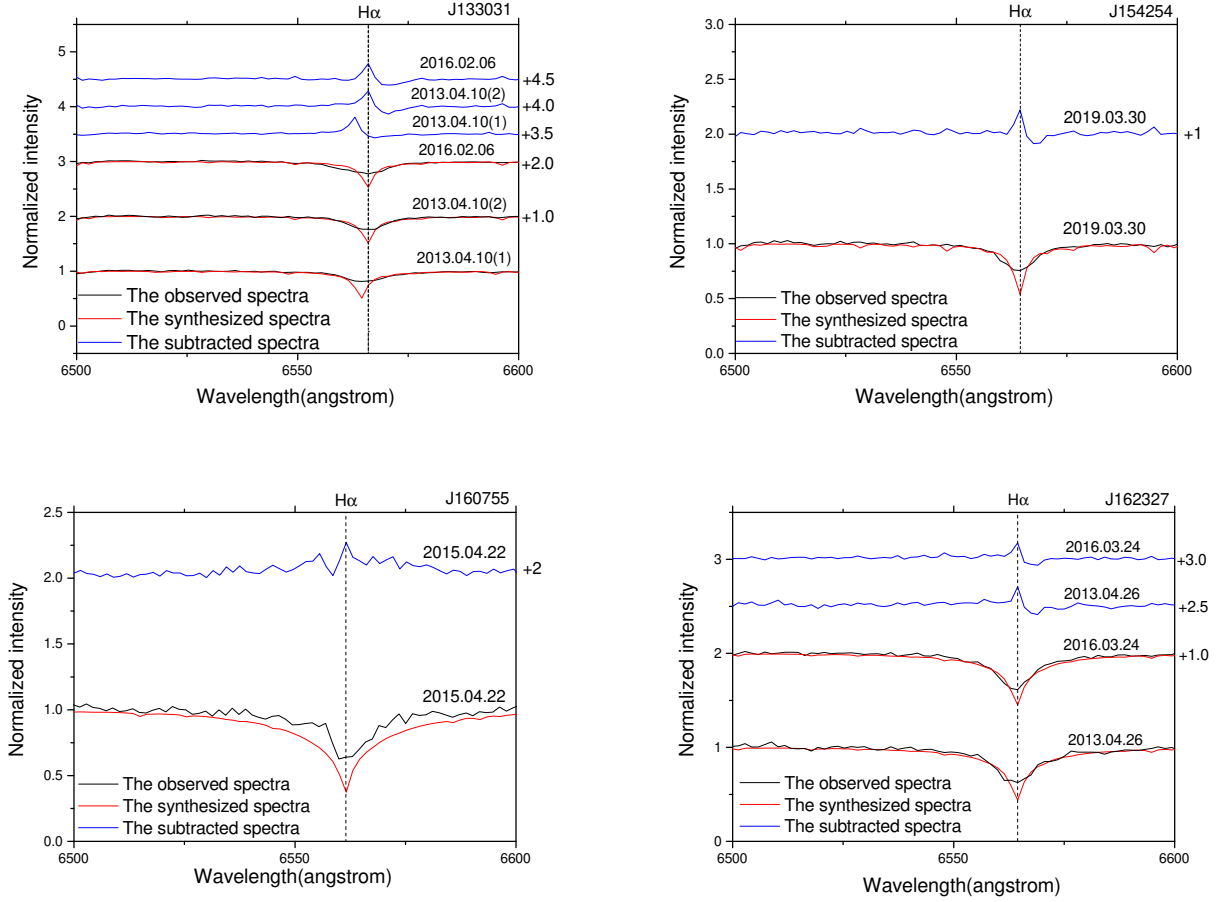
Figure 5. Normalized observed, synthesized and subtracted spectra. The Hα emission line is marked with dotted lines.

Table 9. The basic geometric parameters we obtained and from paper.

| Target | T_1 | | T_2 | | i | | q | | f | |
	Ours	Sun et al.	Ours	Sun et al.	Ours	Sun et al.	Ours	Sun et al.	Ours	Sun et al.
J133031	5860	5930	6019(12)	5961(71)	88.3(2)	79.38(210)	0.0980(4)	0.09(9)	0.560(27)	0.34(29)
J154254	5885	5837	6067(16)	5938(49)	84.4(3)	83.21(308)	0.0867(2)	0.07(9)	0.943(12)	0.97(38)
J155009	6619	6388	6199(16)	5556(39)	85.7(2)	76.64(180)	0.0815(7)	0.07(9)	0.189(71)	0.70(27)
J155106	7147	7553	6819(21)	6962(94)	74.8(5)	71.70(160)	0.0885(15)	0.07(9)	0.693(124)	0.86(48)
J160755	7987	7697	7476(62)	7287(69)	74.9(6)	72.59(105)	0.0991(23)	0.09(9)	0.361(36)	0.48(31)
J162327	6914	7186	6380(18)	5845(58)	82.5(4)	78.67(131)	0.0968(8)	0.09(9)	0.274(64)	0.52(22)
J164000	7137	6740	6574(18)	5805(58)	83.5(2)	75.14(181)	0.0951(7)	0.09(9)	0.287(60)	0.20(49)
J170307	5433	5451	5237(15)	5516(45)	75.7(4)	74.74(162)	0.0930(12)	0.07(9)	0.698(86)	0.08(22)
J223837	6919	7171	6756(25)	6686(55)	74.0(3)	75.41(125)	0.0933(11)	0.09(9)	0.449(78)	-0.12(32)
J224827	6077	5930	5541(27)	5785(75)	83.2(6)	78.01(250)	0.0791(4)	0.07(9)	0.916(22)	0.16(45)
J234634	5851	5816	5746(13)	5957(59)	74.6(3)	77.77(145)	0.0855(6)	0.07(9)	0.373(56)	-0.08(39)

systems were determined. According to the Kepler's third law,

$$M_1 + M_2 = 0.0134A^3/P^2 \qquad (5)$$

the semi-major axis was obtained. The absolute parameters calculated by the above steps and errors on basis of error transfer formulas are shown in Table 10.

The periods of J155109, J170307, J223837, J224827 and J234634 are slowly increasing, and of J154254, J155106 and J164000 are slowly decreasing. There are many explanations about the changes in period. The long-term increase in period can be explained by materials transfer from the less massive component to the more massive component. The long-term decrease in period can be explained by three reasons:

Table 10. The absolute parameters of eleven targets.

Target	M_1 ($M_\odot$)	M_2 ($M_\odot$)	R_1 ($R_\odot$)	R_2 ($R_\odot$)	L_1 ($L_\odot$)	L_2 ($L_\odot$)	A ($R_\odot$)
J133031	1.162(0.254)	0.114(0.026)	1.237(0.121)	0.459(0.049)	2.018(0.605)	0.271(0.079)	2.059(0.015)
J154254	1.317(0.281)	0.114(0.025)	1.464(0.139)	0.514(0.054)	3.215(0.947)	0.389(0.112)	2.379(0.017)
J155009	1.599(0.321)	0.130(0.028)	1.882(0.170)	0.644(0.065)	6.429(1.835)	0.737(0.205)	3.015(0.023)
J155106	1.384(0.290)	0.122(0.028)	1.559(0.148)	0.552(0.059)	3.806(1.128)	0.468(0.135)	2.537(0.019)
J160755	1.310(0.275)	0.130(0.030)	1.445(0.138)	0.537(0.058)	3.053(0.909)	0.414(0.119)	2.394(0.017)
J162327	1.612(0.311)	0.156(0.032)	1.888(0.163)	0.695(0.067)	6.337(1.725)	0.873(0.224)	3.097(0.023)
J164000	1.402(0.287)	0.133(0.028)	1.580(0.144)	0.577(0.058)	3.912(1.109)	0.512(0.142)	2.596(0.019)
J170307	1.134(0.253)	0.105(0.024)	1.204(0.120)	0.436(0.048)	1.874(0.572)	0.271(0.072)	1.985(0.014)
J223837	1.541(0.306)	0.144(0.030)	1.784(0.159)	0.646(0.064)	5.463(1.534)	0.704(0.192)	2.916(0.022)
J224827	1.233(0.274)	0.098(0.022)	1.350(0.134)	0.456(0.050)	2.613(0.802)	0.292(0.087)	2.171(0.016)
J234634	1.141(0.258)	0.098(0.023)	1.218(0.123)	0.425(0.047)	1.953(0.607)	0.233(0.071)	1.984(0.014)

materials transfer from the more massive component to the less massive component, the angular momentum loss or their combined effect. If the changes in period is caused by the materials transfer, the materials transfer rate can be calculated using the following equation,

$$\frac{dM_1}{dt} = \frac{M_1 M_2}{3P(M_1 - M_2)} \times \frac{dP}{dt} \tag{6}$$

The results are shown in Table 8. To further determine the cause of the long-term period decrease, we calculated the timescale τ and the thermal timescale τ_{th} of the materials transfer rate. Using the following equation,

$$\tau = \frac{M_1}{\frac{dM_1}{dt}} \tag{7}$$

the timescale τ of the materials transfer rate was calculated and shown in Table 8. Assuming constant angular momentum and the total mass and using the following equation,

$$\tau_{th} = \frac{GM_1^2}{R_1 L_1} \tag{8}$$

the thermal timescale τ_{th} was calculated and also shown in Table 8. The timescale τ and the thermal timescale τ_{th} of the materials transfer rate are quite different, meaning that the long-term orbital period decrease may be caused by the angular momentum loss.

Chromospheric activity and starspot activity, triggered by magnetic fields and maintained by a magnetic dynamo, are the common phenomena in contact binaries (Long et al. 2018). We noticed that the chromospheric activity indicators of Hα line show emissions. According to Table 3, we found the equivalent widths of the Hα emission line are all greater 0.75Å. Comparing the criteria for the chromospheric activity derived by West et al. (2015), J133031, J154254, J160755, J162327 were determined to exhibit chromospheric activity.

To further understand the evolutionary status of the eleven contact binaries, their mass-luminosity (left) and mass-radius distributions (right) are plotted, shown in Fig. 6. The filled symbols denote the primary components and the open symbols denote the secondary components. The zero-age main sequence (ZAMS) and terminal-age main sequence (TAMS) lines (Hurley et al. 2002) are represented by solid and dashed lines, respectively. The eleven targets are very close in the two figures, meaning that the evolution states of them are similar. The primary component is located between ZAMS and TAMS, indicating that the primary component is still in the main sequence evolution stage. The secondary components are above TAMS, indicating that they are over-luminous, and the reason is that energy transfer from the primary has raised their temperature to the level of that of the primary and increased their luminosity to a value much larger than what would be expected for their mass and size. Hut (1980) proposed that the contact binary instability (Darwin's instability) occurs when $J_o \geqslant 3J_s$. To determine whether the eleven contact binaries are in stable state, J_s/J_o is calculated according to the equation (Li & Zhang 2006),

$$\frac{J_s}{J_o} = \frac{1+q}{q}[(k_1 r_1)^2 + q((k_1 r_1)^2)] \tag{9}$$

where q is the mass ratio, r_1, r_2 is the relative radius, and k_1, k_2 is the dimensionless rotation radius. The value of the dimensionless rotation radius k_1, k_2 depends on the internal structure of the star, so using the accurate dimensionless rotation radius is important to correctly calculate the value of J_s/J_o. Assuming $k_1^2 = k_2^2 = 0.06$, as Rasio (1995) and Li & Zhang (2006), J_s/J_o of the eleven contact binaries were calculated and the results are listed in Table 10. J_s/J_o of of the eleven contact binaries are all less than 1/3, so all of them should be in stable state. In fact, the value of k_1, k_2 can be further precise. The secondary component of contacat binaries approaching merger is a very low mass star, so the totally convective n=1.5 polytrope would be appropriate and $k^2 = 0.205$ (Arbutina 2007). It is a good assumption for a very low mass star ($M_2 < 0.3\ M_\odot$). We reestimated k_1 for primary component of different masses, using the tabulated results from Landin et al. (2009), which considers the effects of tidal and rotational distortions on a star in binary systems. We calculated k_1 using the following linear relationships, $k_1 = -0.250M + 0.539$ for stars with mass in 0.5-1.4 $M_\odot$, $k_1 = 0.014M + 0.152$ for stars with mass more than 1.4 $M_\odot$. After re-determining k_1, k_2, we calculated J_s/J_o again and the results are also listed in Table 10.

We calculated the instability parameters using a series of derivations from Wadhwa et al. (2021), adopting the stability criterion $dJ_T/dJ_A = 0$.

Table 11. The instability parameters of the eleven targets.

Target	J_S/J_O $(k_1 = k_2)$	J_S/J_O $(k_1 \neq k_2)$	q_{inst}	A_{inst} $(R_\odot)$	P_{inst} (d)
J133031	0.24	0.26	0.0847	1.943	0.2774
J154254	0.29	0.22	0.0679	2.097	0.2939
J155009	0.29	0.16	0.0418	2.418	0.3310
J155106	0.28	0.18	0.0595	2.096	0.2861
J160755	0.24	0.18	0.0651	2.007	0.2744
J162327	0.24	0.13	0.0416	2.329	0.3095
J164000	0.25	0.13	0.0558	1.937	0.2519
J170307	0.26	0.29	0.0903	1.959	0.2852
J223837	0.26	0.14	0.0463	2.213	0.2935
J224827	0.32	0.29	0.0782	2.138	0.3136
J234634	0.28	0.31	0.0857	2.026	0.2999
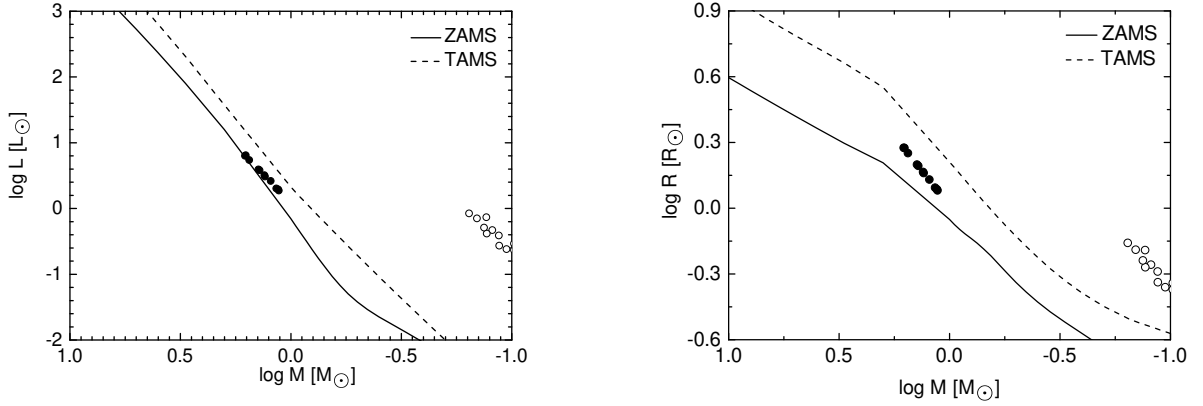
Figure 6. The mass – luminosity diagram (left) and the mass – radius diagram (right).

There is a linear relationship between f and q_{inst} for stars of different masses. After obtaining the values for $f = 1$ and $f = 0$ using the Equation (14), (15) in Wadhwa et al. (2021), the instability mass ratio for any given fill-out factors can be obtained. The instability seperation can be obtained by the Equations (7), (8), (10) in Wadhwa et al. (2021). After getting the instability seperation, the instability period can be calculated by the Kepler's third law. These instability parameters calculated by the above steps are shown in Table 11.

In the spectral class range from F0 to M0 (most contact binaries are this range), the earlier spectral class of systems may become unstable at extremely low mass ratios while the later class of systems may become unstable at mass ratios close to 0.25 (Wadhwa et al. 2021). The spectral types of the eleven contact binaries are near the F type, and their mass ratios are all less than 0.1, and they are extremely low mass ratios, so they can be recognized as pre-merger candidates. Especially, the mass ratio, semi-major axis and period of J234634 exceeded the instability value calculated by the theoretical equations, so we argued that J234634 is on the verge of a merger. The eleven contact binaries have important research significance, therefore it is necessary to monitor them continuously in the future.

DATA AVAILABILITY

The TESS data are publicly available at http://archive.stsci.edu/tess/bulk downloads.html. The ASAS-SN data are publicly available at https://asas-sn.osu.edu/variables/lookup. The SuperWASP data are publicly available at https://wasp.cerit-sc.cz/search. The CSS data are publicly available at https://catalina.lpl.arizona.edu/search/node. The ZTF data are publicly available at https://www.ztf.caltech.edu/ztf-public-releases.html.

REFERENCES

Arbutina B., 2007, MNRAS, 377, 1635
Arbutina B., 2009, MNRAS, 394, 501
Babusiaux C., et al., 2022, arXiv e-prints, p. arXiv:2206.05989
Barden S. C., 1984, in Bulletin of the American Astronomical Society. p. 893
Barden S. C., 1985, ApJ, 295, 162
Bellm E. C., et al., 2018, Publications of the Astronomical Society of the Pacific, 131, 018002
Binnendijk L., 1970, Vistas in Astronomy, 12, 217
Butters O. W., et al., 2010, A&A, 520, L10
Caton D., Gentry D. R., Samec R. G., Chamberlain H., Robb R., Faulkner D. R., Hill R., 2019, PASP, 131, 054203
Christopoulou P. E., Papageorgiou A., 2013, AJ, 146, 157
Christopoulou P.-E., Lalounta E., Papageorgiou A., Ferreira Lopes C. E., Catelan M., Drake A. J., 2022, MNRAS, 512, 1244
Cui X.-Q., et al., 2012, Research in Astronomy and Astrophysics, 12, 1197
Cutri R. M., et al., 2003, VizieR Online Data Catalog, p. II/246
Drake A. J., et al., 2014, ApJS, 213, 9
Du B., et al., 2016, ApJS, 227, 27
Eggleton P. P., Kiseleva-Eggleton L., 2001, ApJ, 562, 1012
Eggleton P. P., Kisseleva-Eggleton L., 2006, Ap&SS, 304, 75
Eker Z., 1999, Turkish Journal of Physics, 23, 357
Eker Z., et al., 2008, MNRAS, 389, 1722
Er-gang Z., Sheng-bang Q., Soonthornthum B., Poshyachinda S., Xiao Z., Sarotsakulchai T., Jia Z., Wen-ping L., 2019, ApJ, 871, L10
Gaia Collaboration et al., 2016, A&A, 595, A1

Gaia Collaboration et al., 2022, arXiv e-prints, p. arXiv:2208.00211
Gazeas K. D., 2009, Communications in Asteroseismology, 159, 129
Green G. M., Schlafly E., Zucker C., Speagle J. S., Finkbeiner D., 2019, ApJ, 887, 93
Hall J. C., 2008, Living Reviews in Solar Physics, 5, 2
Henden A. A., Levine S., Terrell D., Welch D. L., 2015, in American Astronomical Society Meeting Abstracts #225. p. 336.16
Hu S.-M., Han S.-H., Guo D.-F., Du J.-J., 2014, Research in Astronomy and Astrophysics, 14, 719
Hurley J. R., Tout C. A., Pols O. R., 2002, MNRAS, 329, 897
Hut P., 1980, A&A, 92, 167
Jiang D., Han Z., Wang J., Jiang T., Li L., 2010, MNRAS, 405, 2485
Kaluzny J., 1990, Acta Astron., 40, 61
Kaluzny J., Shara M. M., 1988, AJ, 95, 785
Kochanek C. S., Adams S. M., Belczynski K., 2014, MNRAS, 443, 1319
Kochanek C. S., et al., 2017, PASP, 129, 104502
Landin N. R., Mendes L. T. S., Vaz L. P. R., 2009, A&A, 494, 209
Li L., Zhang F., 2006, MNRAS, 369, 2001
Li K., Hu S., Chen X., Guo D., 2017, PASJ, 69, 79
Li K., Xia Q. Q., Hu S. M., Guo D. F., Chen X., 2018, PASP, 130, 074201
Li K., Kim C.-H., Xia Q.-Q., Michel R., Hu S.-M., Gao X., Guo D.-F., Chen X., 2020, AJ, 159, 189
Li K., et al., 2021a, AJ, 162, 13
Li K., Xia Q.-Q., Kim C.-H., Hu S.-M., Guo D.-F., Jeong M.-J., Chen X., Gao D.-Y., 2021b, ApJ, 922, 122
Li K., Gao X., Liu X.-Y., Gao X., Li L.-Z., Chen X., Sun G.-Y., 2022, AJ, 164, 202
Liao W. P., Qian S. B., Sarotsakulchai T., 2019, AJ, 157, 207
Liu L., 2021, PASP, 133, 084202
Long L., Zhang L.-Y., Han X. L., Lu H.-P., Pi Q.-f., Yue Q., 2018, AJ, 156, 220
Lucy L. B., 1968, ApJ, 151, 1123
Luo A. L., et al., 2015, Research in Astronomy and Astrophysics, 15, 1095
Maceroni C., van't Veer F., 1996, A&A, 311, 523
Masci F. J., et al., 2018, Publications of the Astronomical Society of the Pacific, 131, 018003
Mateo M., Harris H. C., Nemec J., Olszewski E. W., 1990, AJ, 100, 469
Mazur B., Krzeminski W., Kaluzny J., 1999, Acta Astron., 49, 551
McCarthy P. J., Kapahi V. K., van Breugel W., Persson S. E., Athreya R., Subrahmanya C. R., 1996, ApJS, 107, 19
Mochnacki S. W., 1981, ApJ, 245, 650
Montes D., de Castro E., Fernandez-Figueroa M. J., Cornide M., 1995, A&AS, 114, 287
Pi Q.-f., Zhang L.-y., Bi S.-l., Han X. L., Lu H.-p., Yue Q., Long L., Yan Y., 2019, ApJ, 877, 75
Pribulla T., Kreiner J. M., Tremko J., 2003, Contributions of the Astronomical Observatory Skalnate Pleso, 33, 38
Qian S., 2003, MNRAS, 342, 1260
Qian S. B., Yang Y. G., Soonthornthum B., Zhu L. Y., He J. J., Yuan J. Z., 2005a, AJ, 130, 224
Qian S. B., Zhu L. Y., Soonthornthum B., Yuan J. Z., Yang Y. G., He J. J., 2005b, AJ, 130, 1206
Qian S.-B., He J.-J., Zhang J., Zhu L.-Y., Shi X.-D., Zhao E.-G., Zhou X., 2017, Research in Astronomy and Astrophysics, 17, 087
Qian S. B., Zhang J., He J. J., Zhu L. Y., Zhao E. G., Shi X. D., Zhou X., Han Z. T., 2018, ApJS, 235, 5
Rasio F. A., 1995, ApJ, 444, L41
Rasio F. A., Shapiro S. L., 1995, ApJ, 438, 887
Ricker G. R., et al., 2014, in Oschmann Jacobus M. J., Clampin M., Fazio G. G., MacEwen H. A., eds, Society of Photo-Optical Instrumentation Engineers (SPIE) Conference Series Vol. 9143, Space Telescopes and Instrumentation 2014: Optical, Infrared, and Millimeter Wave. p. 914320 (arXiv:1406.0151), doi:10.1117/12.2063489
Rubenstein E. P., Bailyn C. D., 1996, AJ, 111, 260
Rucinski S. M., 1994, J. R. Astron. Soc. Canada, 88, 252
Rucinski S. M., 2002, PASP, 114, 1124
Rucinski S. M., Lu W., Mochnacki S. W., Ogłoza W., Stachowski G., 2001, AJ, 122, 1974
Shappee B. J., et al., 2014, ApJ, 788, 48
Sun W., Chen X., Deng L., de Grijs R., 2020, ApJS, 247, 50
Terrell D., 2022, Galaxies, 10, 8
Terrell D., Wilson R. E., 2005, Ap&SS, 296, 221
Tylenda R., et al., 2011, A&A, 528, A114
Vilhu O., 1982, A&A, 109, 17
Wadhwa S. S., De Horta A., Filipović M. D., Tothill N. F. H., Arbutina B., Petrović J., Djurašević G., 2021, MNRAS, 501, 229
Webbink R. F., 1976, ApJ, 209, 829
West A. A., Weisenburger K. L., Irwin J., Berta-Thompson Z. K., Charbonneau D., Dittmann J., Pineda J. S., 2015, ApJ, 812, 3
Wilson O. C., 1978, ApJ, 226, 379
Wilson R. E., 1979, ApJ, 234, 1054
Wilson R. E., 1990, ApJ, 356, 613
Wilson R. E., Devinney E. J., 1971, ApJ, 166, 605
Yan L., Mateo M., 1994, AJ, 108, 1810
Zhao G., Zhao Y.-H., Chu Y.-Q., Jing Y.-P., Deng L.-C., 2012, Research in Astronomy and Astrophysics, 12, 723
Zhou X., Qian S. B., Zhang J., Jiang L. Q., Zhang B., Kreiner J., 2016, ApJ, 817, 133
Zola S., et al., 2004, Acta Astron., 54, 299
Zwitter T., Munari U., Marrese P. M., Prša A., Milone E. F., Boschi F., Tomov T., Siviero A., 2003, A&A, 404, 333
van Hamme W., 1993, AJ, 106, 2096

Table A1. Our photometric data.

Target	HJD-V	ΔMAG-V	HJD-R	ΔMAG-R	HJD-I	ΔMAG-I
J133031	2459322.98762	-0.211	2459322.98847	-0.199	2459322.98900	-0.205
	2459322.98980	-0.228	2459322.99065	-0.211	2459322.99118	-0.206
	2459322.99199	-0.248	2459322.99284	-0.219	2459322.99337	-0.225
	2459322.99418	-0.258	2459322.99502	-0.249	2459322.99555	-0.209
	2459322.99650	-0.271	2459322.99741	-0.250	2459322.99794	-0.234

This table is available in its entirety in machine-readable form in the online version of this article.

von Zeipel H., 1924, MNRAS, 84, 665

APPENDIX A: OUR PHOTOMETRIC DATA

This paper has been typeset from a TEX/LATEX file prepared by the author.